ACS APPLIED MATERIALS & INTERFACES

Research Article

www.acsami.org

Electrochemical Imprinted Polycrystalline Nickel–Nickel Oxide Half-Nanotube-Modified Boron-Doped Diamond Electrode for the Detection of L-Serine

Wei Dai,[†,§] Hongji Li,[*,‡] Mingji Li,[*,†] Cuiping Li,[†] Xiaoguo Wu,[†] and Baohe Yang[†]

[†]Tianjin Key Laboratory of Film Electronic and Communication Devices, School of Electronics Information Engineering, and [‡]Tianjin Key Laboratory of Organic Solar Cells and Photochemical Conversion, School of Chemistry & Chemical Engineering, Tianjin University of Technology, Tianjin 300384, P.R. China

[§]School of Precision Instrument and Optoelectronics Engineering, Tianjin University, Tianjin 300072, P.R. China

Supporting Information

ABSTRACT: This paper presents a novel and versatile method for the fabrication of half nanotubes (HNTs) using a flexible template-based nanofabrication method denoted as electrochemical imprinting. With use of this method, polycrystalline nickel and nickel(II) oxide (Ni–NiO) HNTs were synthesized using pulsed electrodeposition to transfer Ni, deposited by radio frequency magnetron sputtering on a porous polytetrafluoroethylene template, onto a boron-doped diamond (BDD) film. The Ni–NiO HNTs exhibited semicircular profiles along their entire lengths, with outer diameters of 50–120 nm and inner diameters of 20–50 nm. The HNT walls were formed of Ni and NiO nanoparticles. A biosensor for the detection of L-serine was fabricated using a BDD electrode modified with Ni–NiO HNTs, and the device demonstrated satisfactory analytical performance with high sensitivity (0.33 μA μM^{-1}) and a low limit of detection (0.1 μM). The biosensor also exhibited very good reproducibility and stability, as well as a high anti-interference ability against amino acids such as L-leucine, L-tryptophan, L-cysteine, L-phenylalanine, L-arginine, and L-lysine.

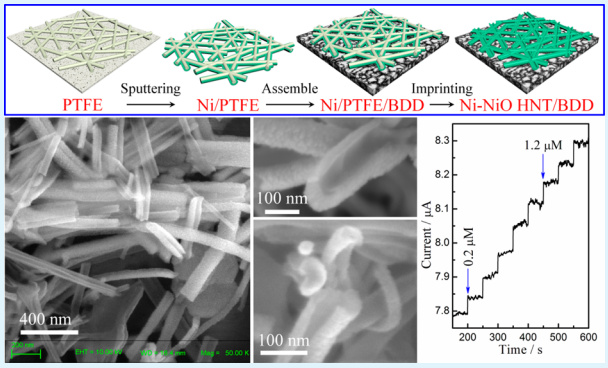

KEYWORDS: *nickel half-nanotubes, boron-doped diamond, pulse electrochemical deposition, biosensor, L-serine*

1. INTRODUCTION

One-dimensional (1D) nanostructures, such as tubes, wires, and rods, exhibit special properties, such as large surface areas, short diffusion distances for mass and charge transport, and substantial capacity for volume change, which may contribute to their improved electrochemical properties.[1−5] Half nanotubes (HNTs) are a new class of 1D nanostructures with large specific surface area, excellent catalytic activity, and short ion/charge carrier diffusion distance.[6−8] The use of electrochemical techniques, such as chronoamperometry,[9] chronopotentiometry,[10−12] cyclic voltammetry,[13] and pulsed electrodeposition,[14,15] is very attractive for the fabrication of 1D nanostructures, owing to their low cost, low synthesis temperature, simple process, and environmental friendliness.[12,16,17] Pulsed electrodeposition, in which the applied potential is oscillated at high frequencies, has been used to fabricate nanostructured metals.[14,18−21] This method provides precise and convenient size and shape control. The observation that material attached to a template can be transferred to an electrode by pulsed electrodeposition provides for the development of a new, unreported deposition approach, denoted as electrochemical imprinting. Amino acids are biologically important organic compounds comprising a central chain of amine ($-NH_2$) and carboxylic acid ($-COOH$) functional groups, along with a side chain specific to each amino acid.[22−24] The amino acid L-serine is a key component for the synthesis of the neurotransmitters glycine and D-serine in the brain.[25] Recent research has shown that L-serine and products of its metabolism are essential for cell proliferation and specific functions of the central nervous system.[26] The findings of altered levels of serine and glycine in patients with psychiatric disorders underscore the importance of L-serine in brain development and function. Therefore, the detection of L-serine is very important in clinical chemistry. Electrochemical techniques for analyzing amino acids have received increasing attention because of their remarkable advantages, such as high sensitivity, use of simple instrumentation, low production cost, and fast response speed, compared with other methods, such as capillary electrophoresis, colorimetry, fluorimetry, and mass-spectrometry.[27−30] To this end, electrodes modified by nickel (Ni) and Ni-based compounds offer a promising alternative to biosensor technology due to their high catalytic activity toward

Received: June 25, 2015
Accepted: September 30, 2015
Published: September 30, 2015

DOI: 10.1021/acsami.5b05642
ACS Appl. Mater. Interfaces 2015, 7, 22858−22867

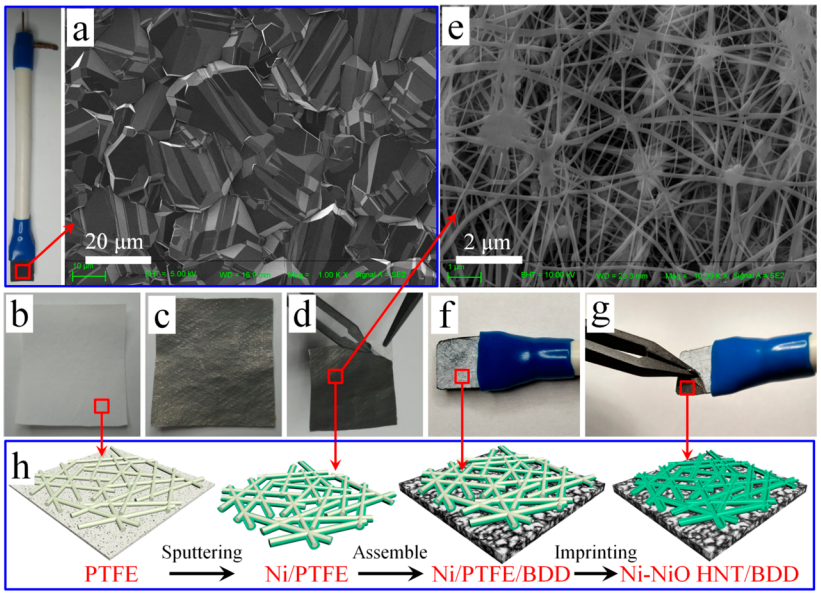

Figure 1. Fabrication processes for Ni−NiO HNTs on a BDD electrode by electrochemical imprinting with a Ni-coated PTFE template. (a) Photograph of the BDD electrode assembly and top-view SEM image of the pristine BDD film. (b) Photograph of the PTFE microporous membrane. (c) Photograph of the Ni−PTFE microporous membrane after magnetron sputtering of a thin Ni layer on the PTFE surface. (d) Removal of the support network from the Ni/PTFE layer. (e) High-magnification SEM image of the Ni/PTFE layer. (f) Photograph of the assembled BDD/Ni/PTFE electrode. (g) Removal of the Ni/PTFE membrane from the imprinted BDD electrode. (h) Schematic illustration of the fabrication processes of the Ni−NiO HNT/BDD electrode.

the electro-oxidation of organics containing OH or NH_2 groups.[27,31−33] Moreover, pure Ni,[34] nickel(II) oxide (NiO),[35] and $Ni(OH)_2$[27,36] nanomaterial-modified electrodes have shown similar electrocatalytic performance in biosensing because their electrocatalytic ability originates from the $Ni(OH)_2$/NiOOH redox couple. Studies on the electro-adsorption and electro-oxidation of amino acids have been mainly conducted using glassy carbon electrodes (GCE)[27,29,37] or carbon-paste electrodes (CPE);[28,38,39] however, strong adsorption and accumulation of intermediate products, electrode fouling, and poor catalytic activity remain considerable problems. Thus, other substrates, such as conductive boron-doped diamond (BDD), are required to overcome these difficulties. BDD electrodes outperform conventional electrodes in terms of stability, chemical inertness, potential window width, and low background current.[40] Combining these superior properties of BDD electrodes with the merits of electrochemical biosensors, such as sensitivity and fast response, amperometric biosensors based on BDD electrodes have attracted the interest of many researchers.[41−44] The use of nickel microparticle modified BDD electrodes was reported by Toghill et al.,[45] with detection limits well in the range of blood glucose levels (and lower) reported. In Hutton et al.'s work, the effect of the size of nickel hydroxide nanoparticles (NPs) on electrocatalytic activity was investigated.[46] Their studies showed that the size of a nanomaterial influences the kinetics of the ion transport, and the intensity of the current signal for the oxidation of glucose is also affected. Thus, the sensitivity of the biosensor will also be affected. Moreover, the synergistic effect of diamond nanowires and nickel nanoparticles could dramatically enhance the electrocatalytic activity toward glucose.[47] The high currents are probably due to a large surface of nanostructures, a three-dimensional effect, the electrocatalytic ability of Ni nanoparticles, and changed mass transport on the electrode. In recent publications, our group has presented the modification of BDD by nanoporous nickel via simple electrodeposition modification, as well as its application to the electrocatalytic oxidation of $_L$-alanine.[31]

We present an electrochemical imprinting approach that is developed for the first time to construct Ni−NiO HNTs. The HNTs were imprinted on a BDD substrate as a biosensor for the detection of $_L$-serine. The fabricated Ni−NiO HNT/BDD electrode biosensor exhibits a wide linear range, low detection limit, and excellent selectivity. The electrode demonstrates better catalytic performance than those modified with bulk materials or other analogical nanomaterials, making the approach more promising for practical applications.

2. EXPERIMENTAL SECTION

2.1. Preparation of Ni−NiO HNT/BDD Electrodes. Self-supporting BDD films (10 mm × 15 mm) were prepared using electron-assisted hot filament chemical vapor deposition. The details of the preparation procedure have been reported elsewhere.[31] The resulting BDD films were adhered to copper rods using a thin copper wire and silver paste. This assembly was mounted in a polyvinyl chloride (PVC) holder, leaving approximately 10 mm × 10 mm BDD exposed, for use as an electrode in subsequent processing (Figure 1a). A scanning electron microscopy (SEM) image of the BDD surface is shown in Figure 1a. As shown in Figure 1b−d, a Ni layer with a thickness of 30−60 nm was deposited by radiofrequency magnetron sputtering on the surface of a porous polytetrafluoroethylene (PTFE) template, which has a spider-like microporous structure, as shown in Figure 1e. The sputtering target was composed of pure Ni (99.999%) with a diameter of 60 mm, and the target-PTFE template distance was 55 mm. After the sputtering chamber had been evacuated to below 1×10^{-4} Pa, high-purity Ar gas (99.999%) was introduced into the chamber up to a pressure of 2 Pa. The radio frequency power was 100 W and the sputtering time was 5 min. After deposition of the Ni layer, the support network was removed from the Ni/PTFE membrane, as shown in Figure 1d. Then the surface of the BDD electrode was covered using a Ni/PTFE membrane, which was sandwiched between two slides, and two each of 1.96 N weights were placed on a slide; thus, the Ni/PTFE membrane was closely attached to the BDD

DOI: 10.1021/acsami.5b05642
ACS Appl. Mater. Interfaces 2015, 7, 22858−22867

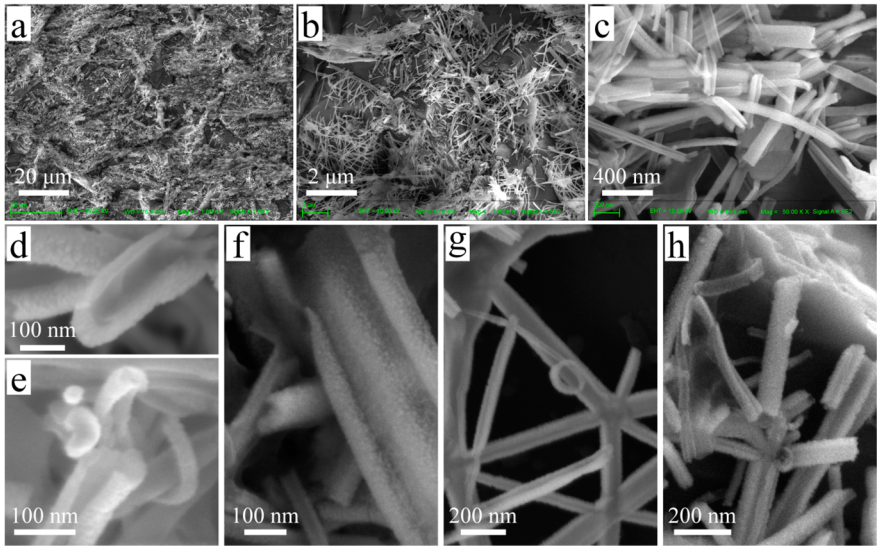

Figure 2. (a) and (b) SEM images of the Ni−NiO HNT/BDD electrode surface. (c) SEM image of Ni−NiO HNTs. (d) and (e) High-magnification SEM images of HNTs. (f) Dual-channel structure of HNTs. (g) and (h) The crossing junction structures of HNTs.

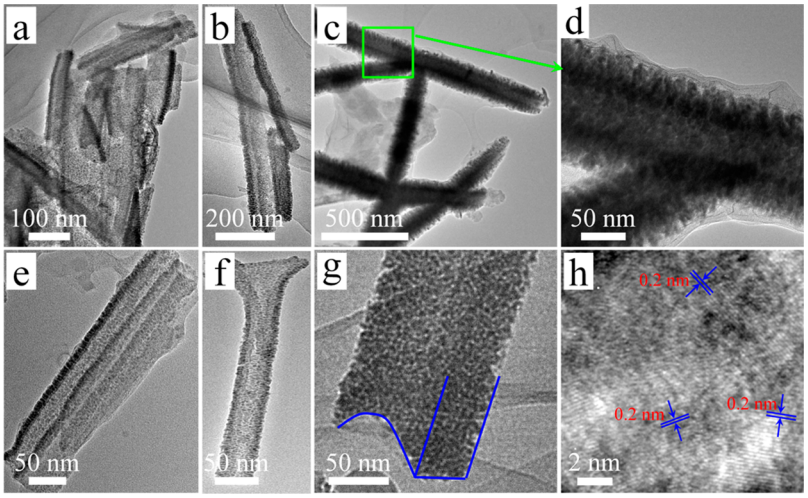

Figure 3. (a) and (b) TEM images of the Ni−NiO HNTs. (c) and (d) Various TEM images of the junctions between HNTs. (e) TEM image of a dual-channel HNT structure. (f) and (g) Single HNTs. (h) High-resolution TEM (HRTEM) image of an HNT wall.

surface by electrostatic adsorption between the Ni/PTFE membrane and BDD film (Figure 1f). For the electrochemical imprinting method used for preparation of the Ni−NiO HNTs on a BDD substrate, a Pt electrode was connected to the reference port, while the BDD electrode with the porous Ni-coated PTFE membrane attached to its surface was connected to the signal port. The electrolyte consisted of an aqueous solution of 4 mM $NiSO_4$ and 0.1 M Na_2SO_4. The distance between the electrodes was 10 mm. The operating conditions for plating were −1.5 V pulse amplitude, 50 Hz pulse frequency (pulse width of 0.01 s), and 50% duty cycle, at a temperature of 25 °C. The pulse electrodepositions were carried out for 10 min. The porous PTFE membrane was subsequently removed from the BDD electrode, as shown in Figure 1g. After the electrode was washed with ultrapure water and dried in a flow of N_2, the Ni−NiO HNT/BDD electrode was finally obtained. All chemical reagents were of analytical grade and used without further purification. The Ni/PTFE membrane has a microporous structure; thus, a Ni^{2+} concentration gradient was produced in the 4 mM M $NiSO_4$ solution, where the highest Ni^{2+} concentration resided near the Ni/PTFE membrane. Figure 1 h shows a schematic illustration of the fabrication processes of the Ni−NiO HNT/BDD electrode. The pulse signal caused the Ni^{2+} in the $NiSO_4$ solution to be reduced to a Ni metal, and Ni layers were consequently deposited onto the BDD electrode. On the other hand, when the pulse electric fields were generated between the BDD electrode and Ni/PTFE membrane, a strong vibration in field strength was produced for the Ni/PTFE membrane. The main reactions in the system can be expressed as follows:

$$Ni^{2+} + 2e^- \rightleftarrows Ni \quad (1)$$

$$BDD + H_2O \rightarrow BDD(\cdot OH) + H^+ + e^{-} \quad (2)$$

$$O_2 + 2H^+ + 2e^- \rightarrow H_2O_2 \quad (3)$$

$$BDD + H_2O_2 \rightarrow BDD(HO_2\cdot) + H^+ + e^- \quad (4)$$

2.2. Material Morphology and Characterization. The obtained samples were characterized by field-emission scanning electron microscopy (FE-SEM; Carl Zeiss MERLIN Compact, Germany; JEOL-6700, Japan), transmission electron microscopy/energy-dispersive X-ray spectrometry (TEM/EDS; JEM-2100, Japan; Philips Tecnai G2 F20, Holland), and X-ray diffraction (XRD; Rigaku D/max-2500/PC, Japan, Cu Kα, λ = 0.15406 nm). The microstructure of the BDD was characterized by Raman spectroscopy (DXR Raman, Thermo Scientific, USA), using a YAG laser (excitation wavelength: 532 nm) as the excitation source. The electrical characteristics of the

DOI: 10.1021/acsami.5b05642
ACS Appl. Mater. Interfaces 2015, 7, 22858−22867

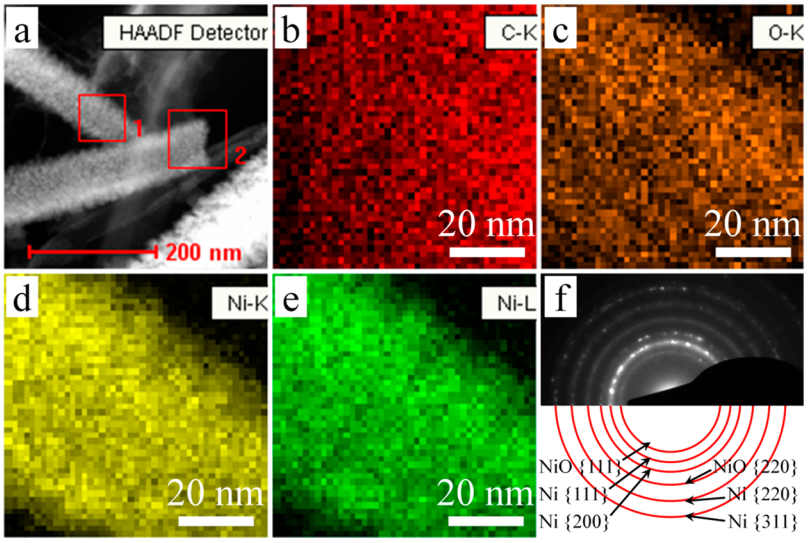

Figure 4. (a) TEM image of Ni−NiO HNTs. (b)−(e) EDS elemental mapping of carbon (b), oxygen (c), and nickel (d), as well as (e) for area 1 marked in (a). (f) SAED pattern of area 2 marked in (a).

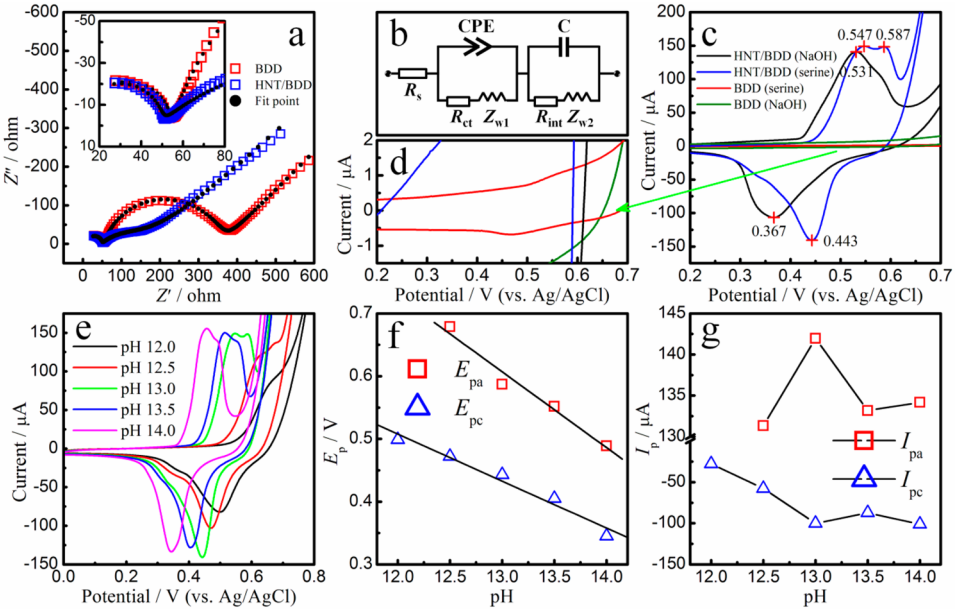

Figure 5. (a) Nyquist plots of the EIS for the bare BDD (red) and Ni−NiO HNT/BDD (blue) electrodes in 0.1 M KCl containing 5 mM $[Fe(CN)_6]^{3-/4-}$ with a frequency range of 0.01−1 × 10^6 Hz and signal amplitude at 0.005 Hz. The inset shows the expanded high-frequency region of the plots (symbols, experimental data; black points, fitting results). (b) The equivalent circuit for data fitting. R_s, the electrolyte resistance; R_{ct}, the charge-transfer resistance at the electrode/electrolyte interface; Z_{W1}, the Warburg impedance accounting for the ion diffusion; CPE, resistance at the Ni−NiO HNT and the double-layer capacitance at the BDD interfaces; R_{int}, the Faradaic reaction impedance at the electrode/electrolyte interface; Z_{W2}, the Warburg impedance accounting for diffuse ion storage at low frequency in the electrode/electrolyte interface; C, capacitance at the Ni−NiO HNT/BDD interface. (c) CV responses of the BDD (red and green) and the Ni−NiO HNT/BDD (blue and black) electrodes at a scan rate of 100 mV s^{-1} in a 0.1 M NaOH (pH 13.0) solution with and without 0.1 mM $_L$-serine. (d) Enlarged CV curve for the bare BDD (red) in a 0.1 M NaOH (pH 13.0) solution with 0.1 mM $_L$-serine. (e) CVs of the Ni−NiO HNT/BDD electrode in N_2-saturated NaOH solutions of different pH: 12.0 (black), 12.5 (red), 13.0 (green), 13.5 (blue), and 14.0 (pink), with a scan rate of 100 mV s^{-1}. (f) Plot of the anodic (E_{pa}) and cathodic peak (E_{pc}) potentials vs pH values. (g) Plot of the anodic and cathodic peak currents vs pH values.

BDD films were investigated using a Hall effect measurement system (HL5550PC, Accent Optical Technologies Ltd., U.K.).

2.3. Electrochemical Characterization. All electrochemical experiments were conducted on a CHI 660E electrochemical workstation (CH Instruments, Chenhua Co., Shanghai, China) using a conventional three-electrode cell. An Ag/AgCl electrode was used as the reference electrode, a platinum wire as the counter electrode, and BDD or Ni−NiO HNT/BDD as the working electrode. Cyclic voltammograms (CVs), electrochemical impedance spectra (EIS), and amperometric response measurements of the samples were investigated. N_2 was bubbled into the electrolytes for 30 min before all cyclic voltammetry experiments, unless stated otherwise. For EIS, the frequency range was 0.01 to 1 × 10^6 Hz, and the amplitude was 0.005 V. All tests were performed at room temperature.

3. RESULTS AND DISCUSSION

The typical grain size of the BDD film after 120 h deposition by HFCVD was found to be ∼30 μm, and its thickness was ∼140

DOI: 10.1021/acsami.5b05642
ACS Appl. Mater. Interfaces 2015, 7, 22858−22867

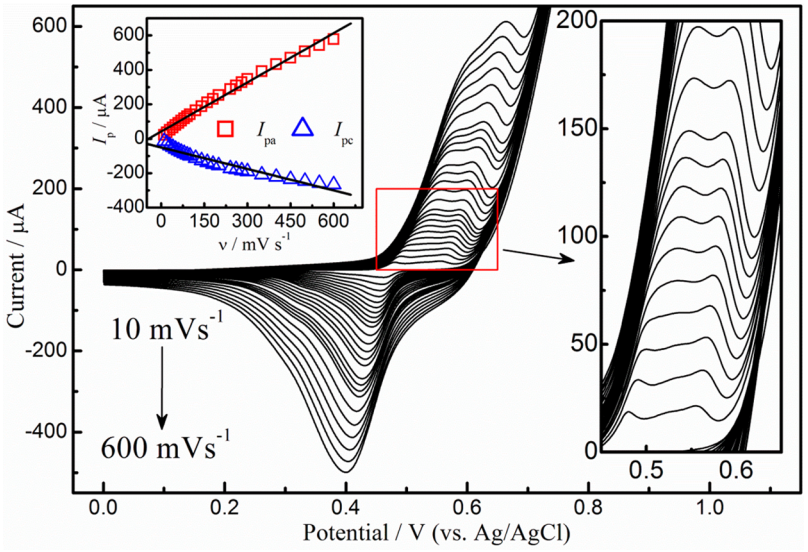

Figure 6. CVs of the Ni−NiO HNT/BDD electrode in a 0.1 M N_2-saturated NaOH (pH 13.0) solution containing 0.1 mM $_L$-serine at different scan rates (from bottom to top: 10, 20, 30, 40, 50, 60, 70, 80, 90, 100, 120, 140, 160, 180, 200, 220, 240, 260, 280, and 300 mV s^{-1}). The inset presents plots of the anodic and cathodic peak currents vs the square root of the scan rates ($\nu^{1/2}$).

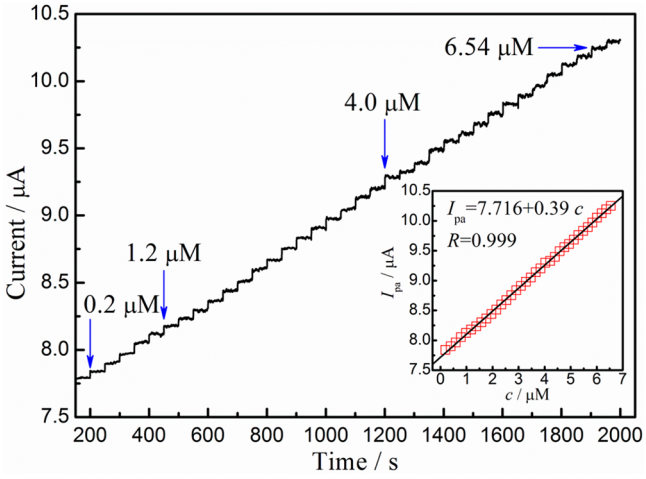

Figure 7. Amperometric response of the Ni−NiO HNT/BDD electrode during successive additions of $_L$-serine into air-saturated, stirred NaOH (0.1 M, pH 13.0) at an applied potential of 0.59 V. The inset presents the calibration curve for the $_L$-serine concentration obtained by the biosensor (symbols, experimental data; line, fitting results).

Table 1. Comparisons with Other Methods for $_L$-Serine Detection

methods	medium	linear range (μM)	LOD (μM)	ref
flow-injection spectrophotometric	alkaline	200−1000	10	59
capillary electrophoresis-in-column light-emitting diode-induced fluorescence detector (γ-cyclodextrin)		0.05−5	0.023	60
electrochemical NiO/GCE	alkaline	1−400	0.85	37
seryl tRNA synthetase coupled with spectrophotometric	pH 8.0	5−100	1.5	61
electrochemical bamboo charcoal/carbon nanosphere electrode	pH 6.8	1−100	0.54	62
electrochemical Ni−NiO HNT/BDD	alkaline	0.2−6.54	0.1	this work

μm (Figure 1b and Figure S1 in the Supporting Information). BDD films grown from randomly oriented nuclei exhibit columnar growth.[48] Hall-effect measurements indicated that the BDD samples are p-type, with a charge carrier mobility of 62.8 $cm^2\ V^{-1}\ s^{-1}$ and a carrier concentration of approximately 6.47 × 10^{19} cm^{-3} at room temperature. The Raman spectrum (Figure S2), XRD pattern (Figure S3), and Hall effect measurement (Figure S4) of the BDD film are indicative of a highly boron-doped conductive diamond film[49,50] with fine crystallinity and a (111) preferred growth orientation.

Figure 2 shows SEM micrographs of the Ni−NiO HNT/BDD electrode surface. As shown in Figure 2a,b, large numbers of 1D nanostructure materials were deposited onto the BDD film via the electrochemical imprinting method. These 1D nanostructures are incomplete nanotubes, or HNTs, and their semicircular-shaped profiles are clearly observable along their entire lengths in Figure 2c−e. Their external diameters are 50−120 nm, consistent with the initial fiber diameters of the PTFE template. In the SEM images shown in Figure 2d−h, the HNTs are observed to have rough surfaces, indicating that the HNT walls were formed by the aggregation of nanoparticles. Moreover, the interconnected HNTs formed dual channels in addition to a crossing junction morphology, as shown in Figures 2f−h, which is beneficial for electrocatalytic activity. This indicates that the resulting HNTs mimic the shape of the PTFE fibers very well.

Figure 3a shows a large number of HNT structures, where the nanotubes exhibit semicircular-shaped profiles along their entire lengths with an outside diameter of approximately 50−120 nm. Figure 3b shows that the HNTs have different lengths and diameters. Because the fibers of the PTFE template are not of a uniform size, the sizes of the HNTs are not consistent. Figure 3c illustrates the morphology of the HNT junctions. Figure 3d shows a magnified TEM image corresponding to the square-marked area in Figure 3c, which reveals a fine-grained polycrystalline structure with a compact texture. Gothard et al. have described a Y-junction morphology for carbon nanotubes and postulated a theory that such "junction" nanotubes should

DOI: 10.1021/acsami.5b05642
ACS Appl. Mater. Interfaces 2015, 7, 22858−22867

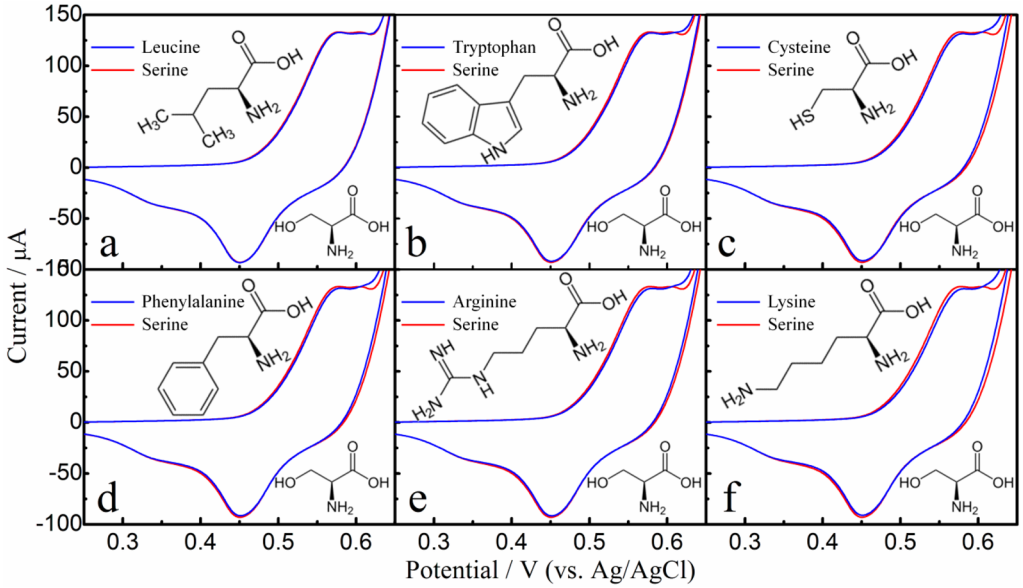

Figure 8. CV responses of the Ni−NiO HNT/BDD electrode to 0.1 mM L-serine and other amino acids as interferents in a 0.1 M NaOH solution at a 100 mV s^{-1} scan rate. Interferents: (a) 0.4 mM L-leucine; (b) 0.4 mM L-tryptophan; (c) 0.4 mM L-cysteine; (d) 0.4 mM L-phenylalanine; (e) 0.4 mM L-arginine; (f) 0.4 mM L-lysine.

exhibit a gating behavior, which serves as an excellent source of ready-made networks for potential nanoscale devices.[51] Figure 3e shows a TEM image of interconnected HNTs with parallel dual channels. The dual channels represent greatly increased connectivity from a single connector for electron transfer. A single HNT with an outside diameter of approximately 50 nm was also observed in the TEM image, as shown in Figure 3f. Figure 3g presents a high-magnification TEM image of the end of an HNT. That the end of the HNT displays a half-moon shape is clearly observable. The HNT wall is formed of nanoscale grains, as indicated by Figure 3h. As shown in Figure 3h, the lattice fringes yield an interplanar spacing of 0.2 nm, corresponding to the distance of the {111} lattice plane of metallic Ni (JCPDS card No. 65-0380).[52] A handful of literature reports have described similar nanostructures, such as Au crescent-shaped HNTs[7] and lithium vanadium oxide HNTs.[6] Thus, Ni nanoparticle-formed HNTs were successfully deposited on the BDD film surface to act as electro-catalysts for the subsequent detection of L-serine.

Figure 4a shows a TEM image of HNTs. Parts (b)−(e), ofFigure 4 respectively display EDS elemental mappings of C (red), O (orange), and Ni (yellow and green) corresponding to the square-marked area 1 in Figure 4a. As observed, the C elemental signal is uniformly distributed over the HNT, which is consistent with the elemental signal of C derived from the supporting film of the copper grid used in the TEM investigation. The O and Ni signals are only distributed in the HNT, and their densities in the center area are lower. The polycrystalline nature of the Ni−NiO HNTs can be confirmed by the selected area electron diffraction (SAED) pattern shown in Figure 4f, which corresponds to the square-marked area 2 in Figure 4a; it shows typical diffraction rings characteristic of the (111), (200), (220), and (311) planes of Ni, as well as diffraction rings characteristic of the (111) and (220) planes of NiO.[53] The EDS elemental mapping analysis and SAED pattern further confirm that Ni−NiO polycrystalline HNTs were prepared.

Figure 5a compares the Nyquist plots of the modified and unmodified BDD electrodes in a 1 M KCl solution containing the redox probe 5 mM $[Fe(CN)_6]^{3-/4-}$ (1:1). The EIS spectra were fitted and simulated using the software ZSimpWin 3.10, and the fitted curves and the Randles equivalent circuit are shown in Figure 5b. The χ^2 values as compared to the model are 5.047×10^{-4} for unmodified BDD and 7.533×10^{-4} for Ni−NiO HNT/BDD. The electrochemical electrode is modeled as an electrolyte resistance (R_s) in series with two parallel circuits, where the first comprises the constant phase element (CPE), the charge-transfer impedance (R_{ct}), and the Warburg impedance (Z_{W1}) and the second comprises the double-layer capacitance (C), the Faradaic reaction impedance (R_{int}), and the Warburg impedance (Z_{W2}). The value of R_{ct} is surface-dependent, with the Ni−NiO HNT/BDD electrode (R_{ct} = 12.18 Ω cm^2) having a lower impedance than the BDD electrode (R_{ct} = 307.6 Ω cm^2), implying that the introduction of the Ni−HNTs plays an important role in providing the conducting bridges for charge transfer. The linear plots in the low-frequency region are ascribed to typical Warburg behavior, which is associated with the diffusion of ions in the electrode/electrolyte interface.

Figure 5c shows the CVs of the BDD and the Ni−NiO HNT/BDD electrodes, taken at a scan rate of 100 mV s^{-1}. In a 0.1 mM L-serine solution (pH 13 NaOH solution supporting electrolyte), the CV curve of the BDD electrode is almost overlapped, but the enlarged CV curve exhibits weak redox peaks located at approximately 0.55 and 0.48 V, respectively, which represent the electrocatalytic signal of the BDD electrode for L-serine (see Figure 5d). The Ni−NiO HNT/BDD electrode exhibits a single clear oxidation peak, a small hump indicative of oxidation, and a reduction peak located at approximately 0.531, 0.580, and 0.367 V, respectively, after repetitive cycling (50 scans) at a scan rate of 100 mV s^{-1} in a 0.1 M NaOH solution for nickel oxide layer passivation. The oxidation peak potential shifted negatively as the number of scans increased. This indicates that the observed redox peaks may originate from the electrochemical reaction of Ni(II)/Ni

DOI: 10.1021/acsami.5b05642
ACS Appl. Mater. Interfaces 2015, 7, 22858−22867

and Ni(III)/Ni(II) redox couples.[34,35,54,55] Ni is first oxidized into Ni(II) to predominantly form $Ni(OH)_2$, and Ni(II) species are further oxidized into Ni(III) as NiO(OH),[56] which is given as follows:

$$NaOH \rightarrow Na^+ + OH^- \quad (5)$$

$$Ni + 2OH^- \rightarrow Ni(OH)_2 + 2e^- \quad (6)$$

$$Ni(OH)_2 + OH^- \rightleftarrows NiO(OH) + H_2O + e^- \quad (7)$$

$$NiO + OH^- \rightarrow NiO(OH) + e^- \quad (8)$$

After 0.1 mM L-serine was added, the obvious oxidation peak and the reduction peak were located at approximately 0.587 and 0.443 V, respectively, suggesting that the Ni−NiO HNTs can mediate L-serine oxidation. The Ni−NiO HNTs act as an enzyme mimicking a catalyst for L-serine oxidation with a possible mechanism directed by Ni(III) with hydrogen and $-NH_2$ liberated[57] as follows:

$$HOCH_2CHNH_2COOH + OH^- \rightarrow HOCH_2CHNH_2COO^- + H_2O \quad (9)$$

$$NiO(OH) + HOCH_2CHNH_2COO^- \rightarrow Ni(OH)_2 + H_3CCOCOO^- + NH_3 \quad (10)$$

In these reactions, strongly oxidizing Ni(III) species oxidize L-serine into pyruvate and are themselves reduced into Ni(II) species at anodic potentials. Therefore, the concentration of Ni(III) decreases while that of Ni(II) increases, causing an increase in the cathodic peak current. The L-serine molecules adsorbed on the surface of $Ni(OH)_2$ can be oxidized at higher potentials parallel to the oxidation of Ni(II) to Ni(III). These two reactions contribute to the observed increase in the anodic peak current. The above results indicate that the Ni−NiO HNTs exhibited an excellent electrocatalytic ability for L-serine oxidation. The excellent detection performance is attributed to the large electroactive surface area, facile electronic transport, and high electrocatalytic activity of the Ni−NiO HNTs, as well as to the synergistic catalytic effect of both Ni−NiO HNTs and the BDD.

It is well-known that pH has a profound effect on the dissociation of L-serine[57] and its amperometric responses. The effect of pH on the response of L-serine at the Ni−NiO HNT/BDD electrode was investigated by obtaining CVs at a scan rate of 100 mV s^{-1} in the pH range of 12.0−14.0, as shown in Figure 5c. The electrode potential of the redox peak was found to be strongly dependent on the pH of the electrolyte, as shown in the inset c1. A linear relationship was obtained between the peak potential and pH in the examined range of 12.0−14.0, suggesting that the electrochemistry of L-serine involved a proton process. This is a consequence of the deprotonation step involved in all oxidation processes facilitated at higher pH values.[58] From inset c2 given in Figure 5c, the oxidation peak current of L-serine is observed to increase as the pH increased from 12.0 to 13.0 and then to decrease as the pH increased from 13.0 to 14.0. Similarly, the reduction peak current increased as the pH increased from 12.0 to 13.0, attaining a maximum at pH 13.0, and then decreased as pH increased from 13.0 to 14.0. Thus, pH 13.0 was chosen as the optimum pH value.

The CVs of the Ni−NiO HNT/BDD electrode in a 0.1 M NaOH solution containing 0.1 mM L-serine at different scan rates were also investigated, as shown in Figure 6. The redox current increased as the scan rate increased from 10 to 600 mV s^{-1} and was found to be proportional to the scan rate (v), indicating that the process is surface-adsorption-controlled. The oxidation peak potential shifted more positively and the reduction peak potential shifted more negatively with increasing scan rate, generating a larger peak-to-peak potential separation. Moreover, the two oxidation peaks gradually merged into a single peak. The oxidation rate of the Ni−NiO HNTs also increased with increasing scan rate.

The current−time response of the Ni−NiO HNT/BDD electrode to L-serine oxidation at a potential of 0.59 V was also studied in N_2-saturated 0.1 M NaOH. In this experimental step, L-serine was sequentially added to the 0.1 M NaOH solution to evaluate the performance of the amino acid sensor, as shown in Figure 7. A calibration equation representing the concentration of L-serine was deduced from a linear regression of the experimental data (I_{pa} (μA) = 7.716 + 0.39c (μM), R = 0.999), as shown in the inset of Figure 7. The linear range for L-serine detection was found to be from 0.20 to 6.54 μM, with a detection limit (LOD) of 0.10 μM (signal/noise = 3) and a sensitivity of 0.33 μA μM^{-1}. In Table 1, some of the analytical characteristics obtained in this work are compared with other methods previously reported for L-serine sensing.[37,59−62] This method is easy to operate, simple, and convenient, suggesting a comparatively lower LOD for L-serine.

Several coexisting amino acids were selected to evaluate the anti-interference ability of the electrode, as shown in Figure 8. No significant interference was observed in the determination of the L-serine concentration (0.1 mM) from the following amino acids: (a) 0.4 mM L-leucine; (b) 0.4 mM L-tryptophan; (c) 0.4 mM L-cysteine; (d) 0.4 mM L-phenylalanine; (e) 0.4 mM L-arginine; and (f) 0.4 mM L-lysine. It was concluded that the effects of small amounts of these amino acids were negligible, suggesting that the prepared Ni−NiO HNT/BDD had a high selectivity toward the nonenzymatic oxidation of L-serine. α-Amino acids consist of a central carbon with an attached amino group ($-NH_2$), carboxylic acid (−COOH), hydrogen atom, and distinctive R groups. The R group, usually referred to as a side chain, determines the properties of the amino acid. The R groups of L-lysine, L-cysteine, and L-arginine can be dissociated and have dissociation constants (pKa) of 10.5, 8.4, and 12.5, respectively; thus, their potential interference is relatively large at pH 13. Figure S7 shows the responses when 0.1 mM L-serine and 0.4 mM L-leucine, 0.4 mM L-tryptophan, 0.4 mM L-cysteine, 0.4 mM L-phenylalanine, 0.4 mM L-arginine, 0.4 mM L-lysine, 0.4 mM L-histidine, 0.4 mM L-alanine, 0.4 mM glucose, and 0.1 mM L-serine were successively added to 0.1 M NaOH. Table S2 summarizes the responses to the interfering substances. Compared to 0.1 mM L-serine, the interfering signals were 4.37%, 3.13%, 6.43%, 2.70%, 7.39%, −7.18%, −12.95%, −74.03%, and −21.47% for the respective species. In short, these substances generated current responses, but even in their presence, the sensor retains good response to L-serine.

The stability of the Ni−NiO HNT/BDD electrode was also examined by recording 100 consecutive CV curves in a 0.1 M NaOH solution (pH 13.0) containing 0.1 mM L-serine at a scan rate of 100 mV s^{-1}. No obvious peak current change was observed (Figure S6a). The reproducibility of the proposed sensor was tested using five different electrodes (Figure S6b). The relative standard deviations of the CV response currents for these specimens were found to be less than 5.0%. Thus, the

DOI: 10.1021/acsami.5b05642
ACS Appl. Mater. Interfaces 2015, 7, 22858−22867

present Ni−NiO HNT/BDD electrode shows high stability and good reproducibility.

4. CONCLUSIONS

Ni−NiO HNTs were synthesized using pulsed electrodeposition to transfer Ni, deposited by radio frequency magnetron sputtering on a porous PTFE template, onto a BDD base electrode in a process denoted as electrochemical imprinting. Our method creates a wealth of opportunities to generate HNTs of metal−metal oxides. An L-serine sensing electrode was fabricated using Ni−NiO HNTs as an electrode modifier and the BDD film as a base electrode. The resulting Ni−NiO HNT/BDD electrode demonstrated excellent electrochemical performance for the detection of L-serine. The developed biosensor exhibited excellent reproducibility, stability, and anti-interference ability and displayed a linear range from 0.20 to 6.54 μM with a low detection limit of 0.10 μM. The excellent sensing properties of the Ni−NiO HNTs/BDD electrodes were shown to be determined by their textural parameters, such as large surface area, facile electronic transport, and high electrocatalytic activity of the Ni−NiO HNTs, as well as by the high stability and low background current of the BDD and the synergistic catalytic effect of the Ni−NiO HNTs and the BDD toward oxidation of L-serine oxidation.

■ ASSOCIATED CONTENT

Supporting Information

Side-view SEM image, Raman spectrum, XRD pattern, and the Hall effect of the pristine BDD; EDS pattern of Ni−NiO HNT/BDD and additional results regarding electrochemical performance. The Supporting Information is available free of charge on the ACS Publications website at DOI: 10.1021/acsami.5b05642.

■ AUTHOR INFORMATION

Corresponding Authors

*E-mail: hongjili@yeah.net (H.L.).
*E-mail: limingji@163.com (M.L.).

Notes

The authors declare no competing financial interest.

■ ACKNOWLEDGMENTS

This work was supported by the Ministry of Science and Technology of the People's Republic of China (No. 2013AA030801), the National Natural Science Foundation of China (Nos. 61301045, 61401306, and 61504096), the Natural Science Foundation of Tianjin City (Nos. 13JCZDJC36000, 15JCYBJC24000), and the Youth Top-notch Talents Program of Tianjin.

■ REFERENCES

(1) Solanki, P. R.; Ali, M. A.; Agrawal, V. V.; Srivastava, A. K.; Kotnala, R. K.; Malhotra, B. D. Highly Sensitive Biofunctionalized Nickel Oxide Nanowires for Nanobiosensing Applications. *RSC Adv.* **2013**, *3*, 16060−16067.

(2) Ren, Y.; Chiam, S. Y.; Chim, W. K. Diameter Dependence of the Void Formation in the Oxidation of Nickel Nanowires. *Nanotechnology* **2011**, *22*, 235606.

(3) Zhou, H.; Zhang, Y. R. Electrochemically Self-Doped TiO_2 Nanotube Arrays for Supercapacitors. *J. Phys. Chem. C* **2014**, *118*, 5626−5636.

(4) Zheng, R. P.; Mo, Z. Y.; Liao, S. J.; Song, H. Y.; Fu, Z. Y.; Huang, P. Y. Heteroatom-Doped Carbon Nanorods with Improved Electrocatalytic Activity toward Oxygen Reduction in an Acidic Medium. *Carbon* **2014**, *69*, 132−141.

(5) Huang, J.; Zhu, Y.; Yang, X.; Chen, W.; Zhou, Y.; Li, C. Flexible 3d Porous CuO Nanowire Arrays for Enzymeless Glucose Sensing: In Situ Engineered Versus Ex Situ Piled. *Nanoscale* **2015**, *7*, 559−569.

(6) Sun, J. L. Synthesis and Electrochemical Properties of Lithium Vanadium Oxides Half Opened-Nanotubes as Cathode of Lithium Ion Batteries. *Mater. Lett.* **2013**, *108*, 193−195.

(7) Qin, Y.; Pan, A.; Liu, L.; Moutanabbir, O.; Yang, R. B.; Knez, M. Atomic Layer Deposition Assisted Template Approach for Electrochemical Synthesis of Au Crescent-Shaped Half-Nanotubes. *ACS Nano* **2011**, *5*, 788−794.

(8) Zhao, S.; Wang, L.; Yang, L.; Chen, Y. Synthesis and Ultraviolet Luminescence Properties of Half-Wall Al_2O_3 Nanotube Arrays. *J. Phys. D: Appl. Phys.* **2009**, *42*, 225106.

(9) Xu, G.; Adeloju, S. B.; Wu, Y.; Zhang, X. Modification of Polypyrrole Nanowires Array with Platinum Nanoparticles and Glucose Oxidase for Fabrication of a Novel Glucose Biosensor. *Anal. Chim. Acta* **2012**, *755*, 100−107.

(10) Saadat, S.; Zhu, J.; Shahjamali, M. M.; Maleksaeedi, S.; Tay, Y. Y.; Tay, B. Y.; Hng, H. H.; Ma, J.; Yan, Q. Template Free Electrochemical Deposition of Znsb Nanotubes for Li Ion Battery Anodes. *Chem. Commun.* **2011**, *47*, 9849−9851.

(11) Shen, C.-M.; Zhang, X.-G.; Li, H.-L. Dc Electrochemical Deposition of CdSe Nanorods Array Using Porous Anodic Aluminum Oxide Template. *Mater. Sci. Eng., A* **2001**, *303*, 19−23.

(12) Ishrat, S.; Maaz, K.; Lee, K. J.; Jung, M.-H.; Kim, G.-H. Nickel Segment-Length Dependent Magnetic Properties of Au-Ni-Au Nanowires at Low Temperature Fabricated by Electrochemical Deposition. *J. Solid State Chem.* **2013**, *199*, 160−163.

(13) Shao, Z.; Li, H.; Li, M.; Li, C.; Qu, C.; Yang, B. Fabrication of Polyaniline Nanowire/TiO_2 Nanotube Array Electrode for Supercapacitors. *Energy* **2015**, *87*, 578−585.

(14) Salem, M. S.; Sergelius, P.; Zierold, R.; Montero Moreno, J. M.; Gorlitz, D.; Nielsch, K. Magnetic Characterization of Nickel-Rich NiFe Nanowires Grown by Pulsed Electrodeposition. *J. Mater. Chem.* **2012**, *22*, 8549−8557.

(15) Mahshid, S. S.; Mahshid, S.; Dolati, A.; Ghorbani, M.; Yang, L.; Luo, S.; Cai, Q. Template-Based Electrodeposition of Pt/Ni Nanowires and Its Catalytic Activity Towards Glucose Oxidation. *Electrochim. Acta* **2011**, *58*, 551−555.

(16) Qiu, R.; Zheng, J. Y.; Cha, H. G.; Jung, M. H.; Lee, K. J.; Kang, Y. S. One-Dimensional Ferromagnetic Dendritic Iron Wire Array Growth by Facile Electrochemical Deposition. *Nanoscale* **2012**, *4*, 1565−1567.

(17) Sada, T.; Fujigaya, T.; Nakashima, N. Design and Fabrication of Ni Nanowires Having Periodically Hollow Nanostructures. *Nanoscale* **2014**, *6*, 11484−11488.

(18) Natter, H.; Schmelzer, M.; Hempelmann, R. Nanocrystalline Nickel and Nickel-Copper Alloys: Synthesis, Characterization, and Thermal Stability. *J. Mater. Res.* **1998**, *13*, 1186−1197.

(19) Natter, H.; Hempelmann, R. Tailor-Made Nanomaterials Designed by Electrochemical Methods. *Electrochim. Acta* **2003**, *49*, 51−61.

(20) Pan, H.; Liu, B.; Yi, J.; Poh, C.; Lim, S.; Ding, J.; Feng, Y.; Huan, C. H. A.; Lin, J. Growth of Single-Crystalline Ni and Co Nanowires Via Electrochemical Deposition and Their Magnetic Properties. *J. Phys. Chem. B* **2005**, *109*, 3094−3098.

(21) Motoyama, M.; Prinz, F. B. Electrodeposition and Behavior of Single Metal Nanowire Probes. *ACS Nano* **2014**, *8*, 3556−3566.

(22) Liu, Q.; Hu, X.; Lin, R.; Sang, W.; Li, S. Limiting Partial Molar Volumes of Glycine, L-Alanine, and L-Serine in Ethylene Glycol + Water Mixtures at 298.15 K. *J. Chem. Eng. Data* **2001**, *46*, 522−525.

(23) Rathgeb, A.; Bohm, A.; Novak, M. S.; Gavriluta, A.; Domotor, O.; Tommasino, J. B.; Enyedy, E. A.; Shova, S.; Meier, S.; Jakupec, M. A.; Luneau, D.; Arion, V. B. Ruthenium-Nitrosyl Complexes with Glycine, L-Alanine, L-Valine, L-Proline, D-Proline, L-Serine, L-

DOI: 10.1021/acsami.5b05642
ACS Appl. Mater. Interfaces 2015, 7, 22858−22867

Threonine, and L-Tyrosine: Synthesis, X-Ray Diffraction Structures, Spectroscopic and Electrochemical Properties, and Antiproliferative Activity. *Inorg. Chem.* **2014**, *53*, 2718−2729.
(24) Ma, Q.; Ai, S.; Yin, H.; Chen, Q.; Tang, T. Towards the Conception of an Amperometric Sensor of L-Tyrosine Based on Hemin/Pamam/Mwcnt Modified Glassy Carbon Electrode. *Electrochim. Acta* **2010**, *55*, 6687−6694.
(25) Yamamoto, T.; Nishizaki, I.; Furuya, S.; Hirabayashi, Y.; Takahashi, K.; Okuyama, S.; Yamamoto, H. Characterization of Rapid and High-Affinity Uptake of L-Serine in Neurons and Astrocytes in Primary Culture. *FEBS Lett.* **2003**, *548*, 69−73.
(26) Tabatabaie, L.; Klomp, L. W.; Berger, R.; de Koning, T. J. L-Serine Synthesis in the Central Nervous System: A Review on Serine Deficiency Disorders. *Mol. Genet. Metab.* **2010**, *99*, 256−262.
(27) Chen, Z. B.; Nai, J. W.; Ma, H.; Li, Z. Q. Nickel Hydroxide Nanocrystals-Modified Glassy Carbon Electrodes for Sensitive L-Histidine Detection. *Electrochim. Acta* **2014**, *116*, 258−262.
(28) Thomas, T.; Mascarenhas, R. J.; D'Souza, O. J.; Martis, P.; Dalhalle, J.; Swamy, B. E. K. Multi-Walled Carbon Nanotube Modified Carbon Paste Electrode as a Sensor for the Amperometric Detection of L-Tryptophan in Biological Samples. *J. Colloid Interface Sci.* **2013**, *402*, 223−229.
(29) Lata, S.; Pundir, C. S. L-Amino Acid Biosensor Based on L-Amino Acid Oxidase Immobilized onto NiHCNFe/c-MWCNT/PPy/GC Electrode. *Int. J. Biol. Macromol.* **2013**, *54*, 250−257.
(30) Chekin, F.; Bagheri, S.; Abd Hamid, S. B. Synthesis of Pt Doped TiO_2 Nanoparticles: Characterization and Application for Electrocatalytic Oxidation of L-Methionine. *Sens. Actuators, B* **2013**, *177*, 898−903.
(31) Dai, W.; Li, M.; Li, H.; Yang, B. Amperometric Biosensor Based on Nanoporous Nickel/Boron-Doped Diamond Film for Electroanalysis of L-Alanine. *Sens. Actuators, B* **2014**, *201*, 31−36.
(32) Lai, X.; Shen, G.; Xue, P.; Yan, B.; Wang, H.; Li, P.; Xia, W.; Fang, J. Ordered Mesoporous Nio with Thin Pore Walls and Its Enhanced Sensing Performance for Formaldehyde. *Nanoscale* **2015**, *7*, 4005−4012.
(33) Gao, H.; Xiao, F.; Ching, C. B.; Duan, H. One-Step Electrochemical Synthesis of PtNi Nanoparticle-Graphene Nanocomposites for Nonenzymatic Amperometric Glucose Detection. *ACS Appl. Mater. Interfaces* **2011**, *3*, 3049−3057.
(34) Wang, B.; Li, S. M.; Liu, J. H.; Yu, M. Preparation of Nickel Nanoparticle/Graphene Composites for Non-Enzymatic Electrochemical Glucose Biosensor Applications. *Mater. Res. Bull.* **2014**, *49*, 521−524.
(35) Yuan, B.; Xu, C.; Deng, D.; Xing, Y.; Liu, L.; Pang, H.; Zhang, D. Graphene Oxide/Nickel Oxide Modified Glassy Carbon Electrode for Supercapacitor and Nonenzymatic Glucose Sensor. *Electrochim. Acta* **2013**, *88*, 708−712.
(36) Kiani, M. A.; Tehrani, M. A.; Sayahi, H. Reusable and Robust High Sensitive Non-Enzymatic Glucose Sensor Based on $Ni(OH)_2$ Nanoparticles. *Anal. Chim. Acta* **2014**, *839*, 26−33.
(37) Roushani, M.; Shamsipur, M.; Pourmortazavi, S. M. Amprometric Detection of Glycine, L-Serine, and L-Alanine Using Glassy Carbon Electrode Modified by Nio Nanoparticles. *J. Appl. Electrochem.* **2012**, *42*, 1005−1011.
(38) Liu, X.; Luo, L. Q.; Ding, Y. P.; Ye, D. X. Poly-Glutamic Acid Modified Carbon Nanotube-Doped Carbon Paste Electrode for Sensitive Detection of L-Tryptophan. *Bioelectrochemistry* **2011**, *82*, 38−45.
(39) Mu, Y.; Jia, D.; He, Y.; Miao, Y.; Wu, H.-L. Nano Nickel Oxide Modified Non-Enzymatic Glucose Sensors with Enhanced Sensitivity through an Electrochemical Process Strategy at High Potential. *Biosens. Bioelectron.* **2011**, *26*, 2948−2952.
(40) Siuzdak, K.; Bogdanowicz, R.; Sawczak, M.; Sobaszek, M. Enhanced Capacitance of Composite TiO_2 Nanotube/Boron-Doped Diamond Electrodes Studied by Impedance Spectroscopy. *Nanoscale* **2015**, *7*, 551−558.
(41) Stefan-van Staden, R.-I.; Nejem, R. a. M.; van Staden, J. F.; Aboul-Enein, H. Y. Amperometric Biosensor Based on Diamond Paste for the Enantioanalysis of L-Lysine. *Biosens. Bioelectron.* **2012**, *35*, 439−442.
(42) Zhou, Y. L.; Zhi, J. F. The Application of Boron-Doped Diamond Electrodes in Amperometric Biosensors. *Talanta* **2009**, *79*, 1189−1196.
(43) Geng, R.; Zhao, G.; Liu, M.; Li, M. A Sandwich Structured SiO_2/Cytochrome C/SiO_2 on a Boron-Doped Diamond Film Electrode as an Electrochemical Nitrite Biosensor. *Biomaterials* **2008**, *29*, 2794−2801.
(44) Zhou, Y. L.; Tian, R. H.; Zhi, J. F. Amperometric Biosensor Based on Tyrosinase Immobilized on a Boron-Doped Diamond Electrode. *Biosens. Bioelectron.* **2007**, *22*, 822−828.
(45) Toghill, K. E.; Xiao, L.; Phillips, M. A.; Compton, R. G. The Non-Enzymatic Determination of Glucose Using an Electrolytically Fabricated Nickel Microparticle Modified Boron-Doped Diamond Electrode or Nickel Foil Electrode. *Sens. Actuators, B* **2010**, *147*, 642−652.
(46) Hutton, L. A.; Vidotti, M.; Patel, A. N.; Newton, M. E.; Unwin, P. R.; Macpherson, J. V. Electrodeposition of Nickel Hydroxide Nanoparticles on Boron-Doped Diamond Electrodes for Oxidative Electrocatalysis. *J. Phys. Chem. C* **2011**, *115*, 1649−1658.
(47) Yang, N. J.; Smirnov, W.; Nebel, C. E. Three-Dimensional Electrochemical Reactions on Tip-Coated Diamond Nanowires with Nickel Nanoparticles. *Electrochem. Commun.* **2013**, *27*, 89−91.
(48) Zhou, D.; Gruen, D. M.; Qin, L. C.; McCauley, T. G.; Krauss, A. R. Control of Diamond Film Microstructure by Ar Additions to CH_4/H_2 Microwave Plasmas. *J. Appl. Phys.* **1998**, *84*, 1981−1989.
(49) Feng, Y.; Lv, J.; Liu, J.; Gao, N.; Peng, H.; Chen, Y. Influence of Boron Concentration on Growth Characteristic and Electro-Catalytic Performance of Boron-Doped Diamond Electrodes Prepared by Direct Current Plasma Chemical Vapor Deposition. *Appl. Surf. Sci.* **2011**, *257*, 3433−3439.
(50) Zou, Y. S.; He, L. L.; Zhang, Y. C.; Li, Z. X.; Wang, H. P.; Gu, L.; Tu, C. J.; Zeng, H. B. Construction and Surface Enhanced Raman Scattering Activity of Gold Nanoparticles Array on Boron Doped Diamond Film. *Mater. Chem. Phys.* **2013**, *141*, 816−821.
(51) Gothard, N.; Daraio, C.; Gaillard, J.; Zidan, R.; Jin, S.; Rao, A. M. Controlled Growth of Y-Junction Nanotubes Using Ti-Doped Vapor Catalyst. *Nano Lett.* **2004**, *4*, 213−217.
(52) Dao, V. D.; Larina, L. L.; Jung, K. D.; Lee, J. K.; Choi, H. S. Graphene-Nio Nanohybrid Prepared by Dry Plasma Reduction as a Low-Cost Counter Electrode Material for Dye-Sensitized Solar Cells. *Nanoscale* **2014**, *6*, 477−482.
(53) Luo, Y.; Zhao, D.; Zhao, Y.; Chiang, F.-k.; Chen, P.; Guo, M.; Luo, N.; Jiang, X.; Miao, P.; Sun, Y.; Chen, A.; Lin, Z.; Li, J.; Duan, W.; Cai, J.; Wang, Y. Evolution of Ni Nanofilaments and Electromagnetic Coupling in the Resistive Switching of Nio. *Nanoscale* **2015**, *7*, 642−649.
(54) Zhang, Y.; Xiao, X.; Sun, Y.; Shi, Y.; Dai, H.; Ni, P.; Hu, J.; Li, Z.; Song, Y.; Wang, L. Electrochemical Deposition of Nickel Nanoparticles on Reduced Graphene Oxide Film for Nonenzymatic Glucose Sensing. *Electroanalysis* **2013**, *25*, 959−966.
(55) Yang, J.; Yu, J.-H.; Strickler, J. R.; Chang, W.-J.; Gunasekaran, S. Nickel Nanoparticle-Chitosan-Reduced Graphene Oxide-Modified Screen-Printed Electrodes for Enzyme-Free Glucose Sensing in Portable Microfluidic Devices. *Biosens. Bioelectron.* **2013**, *47*, 530−538.
(56) Yao, M.; Hu, Z.; Xu, Z.; Liu, Y.; Liu, P.; Zhang, Q. Template Synthesis and Characterization of Nanostructured Hierarchical Mesoporous Ribbon-Like NiO as High Performance Electrode Material for Supercapacitor. *Electrochim. Acta* **2015**, *158*, 96−104.
(57) Quesada-Moreno, M. M.; Aviles-Moreno, J. R.; Marquez-Garcia, A. A.; Partal-Urena, F.; Lopez Gonzalez, J. J. L-Serine in Aqueous Solutions at Different Ph: Conformational Preferences and Vibrational Spectra of Cationic, Anionic and Zwitterionic Species. *J. Mol. Struct.* **2013**, *1046*, 136−146.
(58) Wu, D.; Li, Y.; Zhang, Y.; Wang, P.; Wei, Q.; Du, B. Sensitive Electrochemical Sensor for Simultaneous Determination of Dopamine, Ascorbic Acid, and Uric Acid Enhanced by Amino-Group Function-

DOI: 10.1021/acsami.5b05642
ACS Appl. Mater. Interfaces 2015, 7, 22858−22867

alized Mesoporous Fe_3O_4@Graphene Sheets. *Electrochim. Acta* **2014**, *116*, 244−249.
(59) Yaqoob, M.; Nabi, A. Flow-Injection Method for the Determination of Serine Using Immobilized Enzyme. *Talanta* **2001**, *55*, 1181−1186.
(60) Li, S. T.; Yu, Q. L.; Lu, X.; Zhao, S. L. Determination of D,L-Serine in Midbrain of Parkinson's Disease Mouse by Capillary Electrophoresis with in-Column Light-Emitting Diode Induced Fluorescence Detection. *J. Sep. Sci.* **2009**, *32*, 282−287.
(61) Kugimiya, A.; Matsuzaki, E. Microfluidic Analysis of Serine Levels Using Seryl-Trna Synthetase Coupled with Spectrophotometric Detection. *Appl. Biochem. Biotechnol.* **2014**, *174*, 2527−2536.
(62) Saha, M.; Das, S. Electrochemical Detection of L-Serine and L-Phenylalanine at Bamboo Charcoal−Carbon Nanosphere Electrode. *J. Nanostruct. Chem.* **2014**, *4*, 1−9.

DOI: 10.1021/acsami.5b05642
ACS Appl. Mater. Interfaces 2015, 7, 22858−22867